Check for updates
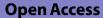
Inhibition of tumor immune escape by blocking PD-1/PD-L1 engagement with dual-targeting molecularly imprinted polymer layer

Wenwen Ji[1], Bei Zhang[1], Xuetong Sun[1], Lijuan Ma[1], Xiangying Zhang[1], Wenhui Qian[1], Wenjuan Fu[1], Jianting Li[1] and Dong Zhu[1*]

*Correspondence:
dongzhu@njucm.edu.cn

[1] School of Pharmacy, Nanjing University of Chinese Medicine, Nanjing 210023, Jiangsu, China

Abstract

Blocking the binding of PD-1/PD-L1 has become an effective strategy in inhibition of tumor immune escape. At present, it mainly depends on the employment of macromolecular antibodies, which target PD-1/PD-L1 protein through binding one of PD-1 or PD-L1 domains. In this study, we present a different strategy, an aptamer modified molecularly imprinted polymer layer (APD–PD-L1–MIPL), to break PD-1/PD-L1 binding for the inhibition of tumor immune escape. The APD–PD-L1–MIPL is prepared by a MIP layer on the surface of $CaCO_3$ nanospheres using the peptide segment of the PD-L1 protein as a template. The subsequent removal of $CaCO_3$ nanospheres core formats the MIP layer, to ensure high specifically matching capacity and short equilibrium time. A PD-L1 antagonistic DNA aptamer, is modified into the MIP layer to enhance recognition capacity, resulting in dual-targeting functionality. The APD–PD-L1–MIPL is able to bind PD-L1 and allow suppressing the engagement of PD-L1 with PD-1, inducing to block of the downstream signaling pathways and, therefore, restore T cell function and inhibition of cancer growth. The APD–PD-L1–MIPL can quantitatively detect the bound proteins and the LOD of APD–PD-L1–MIPL is 0.003 mg mL^{-1}. This strategy enables provide a new idea for tumor immunotherapy.

Keywords: PD-L1, Molecularly imprinted polymer, Aptamer, Cancer immunotherapy monitoring

Introduction

Programmed death receptor 1 (PD-1) is an important T cell receptor immunosuppressive molecules which is mainly expressed on the surface of activated immune T cells. In addition, PD-L1, the corresponding ligand of PD-1, is highly expressed on tumor cells and tumor-infiltrating lymphocytes (Callahan et al. 2013). The binding of PD-1/PD-L1 can inhibit the tumor killing ability of T cells, and cause the tumor immune escape (Li et al. 2018; Zak et al. 2015). PD-1/PD-L1 inhibitors bring a major breakthrough in cancer immunotherapy (Mahoney et al. 2015; Zou et al.

2016). PD-1/PD-L1 inhibitors which have been launched mainly belong to macro-molecular antibody (mAb) drugs. Such as, Nivolumab, a monoclonal antibody, was marketed as a first PD-1/PD-L1 inhibitor targeting PD-1 for treating non-small cell lung cancer (Borghaei et al. 2015). Other macro-molecules such as pembrolizumab, durvalumab and atezolizumab are also approved as treating cancer drugs (Bellmunt et al. 2017; Robert et al. 2015). These macromolecular drugs have made a break-through in the clinical treatment of a variety of tumors, and many cancer patients have extended significantly longer survival and some achieve complete remissions using them. Although the clinical effect of monoclonal antibodies is remarkable, there are still some unavoidable problems. These monoclonal antibodies are prone to cause immune-related adverse reactions, such as thyroid dysfunction, during treatment, and long-term use is prone to drug resistance, which limits their further application (de Filette et al. 2019; Saleh et al. 2020). Moreover, they are also unfavorable to the average patient, because they are expensive and difficult to store and transport.

Molecularly imprinted polymers (MIPs) are artificial recognition polymers which possess special cavities to bind target. MIPs are usually prepared through a polymerizing process of cross-linking monomers around an interested molecule, which is acted as a template. Removing of the template molecule produces a special polymer with cavities complementary in position, shape and size of chemical groups (Gu et al. 2021; Liu et al. 2021). MIPs have been previously used in identification, determination of trace analytes and diagnosis of some diseases (Guo et al. 2021; Haupt et al. 2020; Kimani et al. 2021; Wackerlig et al. 2016). However, using the bulk MIPs for recognition of special protein, un-acquiring binding sites, low imprinting capacity and deep embedding template could lead to target leakage (Pan et al. 2011; Zhu et al. 2010).

In this work, a MIP layer was prepared to block PD-1/PD-L1 engagement and, there-fore, restore the capacity of T cell and restrain the further growth of cancer. As shown in Fig. 1a, the MIP layer on the surface of $CaCO_3$ nanospheres using the peptide seg-ment of the PD-L1 protein as a template was designed to selectively bind to PD-L1 pro-tein, resulting in PD-1/PD-L1 axle inhibition. Uniquely among the above mention mAbs, which usually target PD-1 or PD-L1 by binding one of their domains, the MIP enables target PD-L1 through binding with the amino acid sequence. The mature PD-L1 protein is composed of an extracellular domain of 220 amino acids, and we chose the amino acid sequence that binds to outside membrane of PD-1 as the template sequence. The polymer obtained using this sequence as a template can bind well to the extracellular domain of PD-L1 protein. The removal of $CaCO_3$ nanospheres core enable form the MIP layer, to ensure high specifically matching capacity and short equilibrium time. In addi-tion, a PD-L1 antagonistic DNA aptamer (Lai et al. 2016), aptPD-L1, was modified into the MIP layer to enhance recognition capacity, resulting in dual-targeting functionality. Aptamer is usually regarded as an antibody substitute owing to its excellent capacity of high specific binding affinity, low immunogenicity and easy to be modified for therapeu-tic formulations with various 3D structures (Chen et al. 2011; Kato et al. 2016; Lao et al. 2015; Mayer 2009; Ng et al. 2006; Sun et al. 2014; Wheeler et al. 2011). The resulting APD−PD-L1−MIPL enables recognize and bind to PD-L1 at the cancer cell surface, as confirmed by confocal fluorescent imaging. Remarkably, the APD−PD-L1−MIPL ena-bles break the binding of PD-1/PD-L1, reactivate the suppressed T lymphocytes and
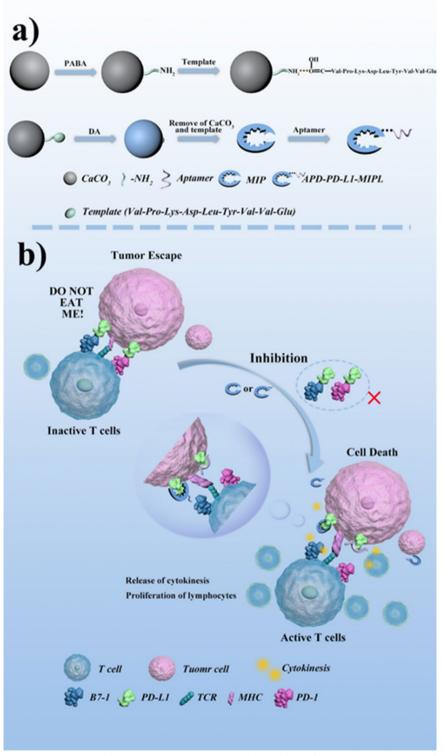
Fig. 1 a Schematic process for APD–PD-L1–MIPL and MIP synthesis. **b** Use of APD–PD-L1–MIPL and MIP for immunotherapy

activate the immune function. Overall, these results show that APD–PD-L1–MIPL have a promising future in cancer therapy and diagnostics.

Materials and methods

Materials

Dopamine (DA) was purchased from Huaxia Reagent. Coomassie Blue Fast Staining Solution were brought from BeyotimeFITC conjugation kit, programmed cell death protein 1 (PD-L1), peptide sequence (sequence: VPK DLY VVE) and aptamer (sequence: 5′-ACGGGCCACATCAACTCATTGATAGACAATGCGTCCACTGCCCGT-3′) were synthesized by Sangon Biotech (Shanghai) Co.

Synthesis of CaCO$_3$ nanoparticles

CaCO$_3$ nanoparticles were prepared via a previous report (Dong et al. 2018). In brief, CaCl$_2$ (1 M) and Na$_2$CO$_3$ (1 M) were mixed in deionized water to make 1 M reserve liquid for reserve. In 400 mL deionized water, slowly add 1 M CaCl$_2$ solution, stir at medium speed for 30 min, quickly add the same amount of Na$_2$CO$_3$ solution and make up the volume to 500 mL, stirring violently for 10 min. Sat at room temperature for 24 h, centrifuge to collect precipitation, wash with deionized water and alcohol, dry and set aside.

Fabrication of APD–PD-L1–MIPL and MIP

The above-mentioned CaCO$_3$ NPs (0.2 g) was dispersed into water for 0.5 h, and 8 mg of pamino benzoic acid (PABA) was added, stirred at 70 °C for 2 h, and thus centrifugal drying was used to obtain NH$_2$ modified CaCO$_3$ NPs (CaCO$_3$@NH$_2$ NPs). PABA can be ionized into p-aminobenzoate in water, which can be adsorbed with Ca^{2+} and uniformly adsorbed on the surface of CaCO$_3$ nanoparticles by high-speed stirring to form CaCO$_3$@NH$_2$.

A short peptide exposed outside the membrane during the binding of PD-1 and PD-L1 was selected as the template molecule (Minouraa et al. 2001). Briefly, 10 mg of CaCO$_3$@NH$_2$ NPs was dispersed in 15 mL Tris–HCl buffer solution (20 mM pH 8.0), and 40 mg of peptide template (VPK DLY VVE) was added and shaken for 3 h. Carboxyl groups on polypeptide sequences are immobilized on CaCO$_3$@NH$_2$ through multiple hydrogen bonding interactions with amino groups (Chen et al. 2019). Then, add DA (20 mg) and ammonium persulfate (APS) and shake at room temperature for 3 h to ensure sufficient air to wrap DA on CaCO$_3$@NH$_2$. The CaCO$_3$ and peptide templates were eluted with 10% HAC-10% SDS mixed solution, and until no absorption was detected at 280 nm (Hao et al. 2016), and the MIP was obtained. NIP without peptide template was also prepared under the same condition.

The aptPD-L1 and MIP were incubated in 25 °C for 2 h, and then aptamer were conjugated onto the surface of dopamine (DA) by π–π stacking and hydrogen bonding (Zhao et al. 2021a; b), and the corresponding APD–PD-L1–MIPL was obtained.

Static recognition experiment

The recognition characteristics of APD–PD-L1–MIPL, MIP and NIP were verified by static recognition experiments. First, 0.1 mg of the APD–PD-L1–MIPL, MIP and NIP

were added to the PD-L1 protein solution (0.2–1 mg mL^{-1}), respectively. The mixture was uniformly dispersed by gently blowing, and the reaction was oscillated for 4 h. Collecting supernatant, and the change of protein concentration before and after reaction was determined by a multifunctional plate reader at 595 nm according to Bradford Protein Assay Kit. The binding amount Q(mg g^{-1}) as follows (1):

$$Q = (C_0 - C)V/m \tag{1}$$

where C_0 (mg mL^{-1}) is the original concentration of PD-L1, C (mg mL^{-1}) represents the protein concentration in the supernatant after recognition, V (L) stands for the volume of the adsorption mixture, and m (g) is the weight of the nanomaterial.

The recognition ability of APD–PD-L1–MIPL was evaluated by the imprinting factor (IF):

$$IF = Q_{APD\text{-}PD\text{-}L1\text{-}MIPL}/Q_{NIP} \tag{2}$$

where $Q_{APD–PD\text{-}L1–MIPL}$ and Q_{NIP} was the binding ability of APD–PD-L1–MIPL and NIP, respectively.

Kinetics recognition experiments

First, 0.1 mg of the APD–PD-L1–MIPL, MIP and NIP were mixed with 0.5 mL of PD-L1 protein solution (0.6 mg mL^{-1}) for different times (30–180 min), respectively. The supernatant was collected by centrifugation. The changes of protein concentration (before and after reaction) were measured by Bradford Protein Assay Kit at 595 nm. The adsorption amount Q and imprinting factor IF were calculated by formula (1) and (2).

Selectivity experiments

Lyz, BSA, β-CN and HRP was selected as competitive proteins to evaluate the selectivity of the APD–PD-L1–MIPL, MIP and NIP. The selectivity of the APD–PD-L1–MIPL, MIP and NIP was described by selection factors (β) (Qian et al. 2021):

$$\beta = IF_{tem}/IF_{refer} \tag{3}$$

where IFt_{em} is the IF value of the template protein, IF_{refer} is the IF value of the selected protein, using Eqs. (1)–(3) to evaluate selective recognition capabilities.

Competitive recognition performance

In the mixed solution of PD-L1, Lyz and BSA, Lyz and BSA were used as competitive proteins to further prove the selectivity of the APD–PD-L1–MIPL and MIP, and qualitative analysis was carried out by SDS–PAGE gel electrophoresis.

Reusability

The APD–PD-L1–MIPL were reused four times to evaluate its reusability in the step of binding–elution–rebinding.

The quantitation of the APD–PD-L1–MIPL

FITC was used to conjugate PD-L1 to achieve the APD–PD-L1–MIPL quantification. Protein and FITC were coupled at a mass ratio of 1 mg:150 μg. Then, purified by

desalting column to obtain high purity coupling product. The ratio of FITC labeled protein was calculated by F/P:

$$F/P = 3.1 \times A_{495}/(A_{280} - 0.31 \times A_{495}) \tag{4}$$

The protein with different concentration after FITC coupling was combined with the same amount of APD–PD-L1–MIPL (0.001 mg), and the relationship between adsorption quantity Q and fluorescence intensity value was studied.

Cell cytotoxicity

The effect of the APD–PD-L1–MIPL and MIPs on cell viability was detected by MTT colorimetric assay. L-02 and B16 F10 were inoculated in 96-well plates. Washing the cells with PBS for three times, the cells were cultured with different concentrations of (0.125, 0.25, 0.5, 1, 2, 4 mg mL^{-1}) the APD–PD-L1–MIPL, MIP and NIP for 24 h, and the culture medium was used as control. Then, incubate with MTT reagent, 37 °C for 4 h, and add DMSO (100 μL), shaking and measure the absorbance of each well at 490 nm with SPARK 10 M multimode plate reader.

Intracellular imaging

Since the APD–PD-L1–MIPL can selectively recognize PD-L1, it is important to verify that they also enable recognize and bind PD-L1 of cancer cells. FITC was modified to the APD–PD-L1–MIPL, MIP and NIP to give fluorescence property. B16 F10 cells with high expression of PD-L1 protein were inoculated in confocal Petri dishes with a diameter of 20 mm and cultured for 24 h. After being cultured with the same amount of the APD–PD-L1–MIPL, MIP and NIP (0.6 mg mL^{-1}) for 2 h, and stained with 500 μL DAPI for 5 min. The images were obtained by inverted confocal microscope (Leica, Germany), and L-02 cells, which did not express PD-L1, were used as control.

Similarly, Hoechst 33258 live cell staining was performed on B16 F10 cells to observe apoptosis. B16 F10 cells were seeded on 6-well plates, and 0.6 mg mL^{-1} of APD–PD-L1–MIPL, MIP and NIP were added after 24 h, and PBS was used as a control for treatment for 24 h. T lymphocytes were extracted from C57BL/6 mice, co-cultured with B16 F10 cells, and anti-CD3 (5 μg mL^{-1}) and CD28 (2 μg mL^{-1}) monoclonal antibodies were added to stimulate cells. Hoechst 33258 live cells were stained and visualized by laser confocal after 30 min incubation.

Flow cytometry

T lymphocytes were extracted from the spleen of C57BL/6 mice, labeled with CFDA-SE, and co-cultured with B16 F10 cells. After treatment with the APD–PD-L1–MIPL, MIP and NIP, cells were re-suspended in PBS and the proliferation of T lymphocytes were observed by flow cytometry.

Hemolysis experiment

To initially assess the feasibility of the APD–PD-L1–MIPL for subsequent intravenous injection administration, hemolytic experimental was also studied. Rat plasma samples were centrifuged, and the red blood cell suspension was re-suspended in physiological saline (2% RBCS). And RBCS (0.08 mL) and saline (0.8 mL) were added as negative

control, 0.08 mL of RBCS and 0.8 mL of distilled water were added as positive control. Then, 0.8 mL of the APD–PD-L1–MIPL with different concentrations (0.2, 0.4, 0.6, 0.8, 1 mg mL^{-1}) was added to 0.08 mL RBCS, respectively. All samples were incubated at 37 °C for 3 h, and their absorbance at 570 nm was determined, and the hemolysis rate was calculated:

$$\text{Hemolysis}\,(\%) = \left(A_{\text{sample}} - A_{\text{negative}}\right)/\left(A_{\text{positive}} - A_{\text{negative}}\right) \times 100\% \tag{5}$$

where A_{sample}, A_{negative} and A_{positive} represent the absorbance values of samples, negative controls and positive controls at 570 nm, respectively.

Results and discussion

Preparation of the APD–PD-L1–MIPL and MIP

The freely accessible peptide Val–Pro–Lys–Asp–Leu–Tyr–Val–Val–Glu which can bind to outside membrane of PD-1 was chosen as a template epitope (Fig. 1a). The synthetic peptide of the PD-L1 epitope, was immobilized onto the amine-functionalized CaCO$_3$ nanospheres. This enables allow the template to be orientation-immobilized around the nanoparticles. Therefore, an MIP layer around CaCO$_3$ nanosphere was endowed by a surface polymerization, which owned uniformly, homogeneous and specific binding sites. The removal of CaCO$_3$ nanospheres core enable form the MIP layer, to ensure high specifically matching capacity and short equilibrium time. Additional file 1: Fig. S1 shows the TEM image of the pure CaCO$_3$ nanoparticle with size of 125 nm. After modification with aminobenzoic acid (PABA), a new infrared absorption peak at 3446 cm^{-1} due to the stretching vibration of N–H, confirmed the successful conjugation of the amine group onto the surface of CaCO$_3$ nanospheres (Additional file 1: Fig. S2). Different dosage of dopamine (DA) leads to the change of the MIP layer thickness (Chen et al. 2019). In Additional file 1: Fig. S3a, the binding quantity of the MIP layer is rising with the increase of DA. The binding quantity reached to maximum with the rate of 1:2 of CaCO$_3$@NH$_2$:DA, and then the imprinting factor IF was higher than 1.9. The low DA dosage leads to thin layer, resulting in weak capacity for recognizing, as the increase of DA ratio, the ability of recognition was improved. While too thick MIP layer due to high DA dosage also induced to long equilibrium time, the mass ratio of 1:2 with CaCO$_3$@NH$_2$:DA as the optimal mass ratio.

Dosage of template molecules are another important factor to affect the binding effect. Different concentrations (0.67, 1.33, 2.00, 2.67, 3.33 mg mL^{-1}) of the template molecules were used to prepare MIP layers, to measure the binding amount of target molecule. In Additional file 1: Fig. S3b, c, with the increase of the template molecules from 0.67 to 3.33 mg mL^{-1}, the binding quantity was increased due to the increasing of the binding site. Meanwhile, the difference in the imprinting time also led to the change of the binding capacity, and when the time was 4 h, the binding capacity was highest. Therefore, the template molecule of 2.67 mg mL^{-1} and the imprinting time of 4 h were the optimal conditions. After acid dissolution the CaCO$_3$ core nanospheres and removal of non-polymerized monomer, the MIP layer was presented high affinity to the peptide. The infrared spectrum also further confirmed the fabrication of the MIP layer, and the new absorption peaks around 3500 cm^{-1} represent O–H and N–H functional groups (Additional file 1: Fig. S2).

The transmission electron microscope (TEM) of the APD–PD-L1–MIPL and MIP are shown in Fig. 2a, b. The MIP exhibited uniform spherical morphology with 200 nm. The APD–PD-L1–MIPL was monodispersed and showed a batch-to-batch repeatable hydrodynamic diameter of 280 nm (Fig. 2c). The pure MIP and NIP charges are about -0.9 mV and -1.3 mV, respectively (Fig. 2d). The phenolic hydroxyl group and amino group maintained the MIP negative charge. When the aptPD-L1aptamer was modified onto the surface of the MIP, the potential became negative to approximately -23.6 mV (Fig. 2d), which is due to the electronegativity of aptamer. No aggregation or changing in the binding characteristics of the APD–PD-L1–MIPL was observed within a period of 1 year when stored at 4 °C.

Binding of APD–PD-L1–MIPL to PD-L1

The in vitro specific recognition of the APD–PD-L1–MIPL to PD-L1 was first evaluated. The saturation binding was conducted at different PD-L1 concentrations (0.2–1.0 mg mL^{-1}) to study the binding ability of the APD–PD-L1–MIPL, MIP layer and NIP. In Fig. 2e, the equilibrium binding isotherm indicated that the APD–PD-L1–MIPL enables bind specifically to PD-L1 protein; meanwhile, a low binding was observed using a non-imprinted polymer (NIP) as control. The binding targets of the APD–PD-L1–MIPL, MIP and NIP were 266.8 mg g^{-1}, 167.1 mg g^{-1} and 64.0 mg g^{-1}. And the corresponding imprinting factor of the APD–PD-L1–MIPL and MIP was 4.2 and 2.6 (Additional file 1: Fig. S4a). This high specific binding of the
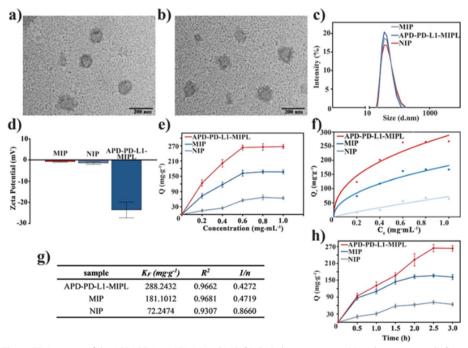

Fig. 2 TEM images of the APD–PD-L1–MIPL (**a**) and MIP (**b**). DLS characterization (**c**) and zeta potential (**d**) of the APD–PD-L1–MIPL, MIP and NIP. **e** Adsorption isotherms of PD-L1 onto the APD–PD-L1–MIPL, MIP and NIP. **f** Scatchard plot of the adsorption assays of PD-L1 on the APD–PD-L1–MIPL, MIP and NIP. **g** Langmuir adsorption constants for binding of PD-L1 on the APD–PD-L1–MIPL, MIP and NIP. **h** Adsorption kinetics of PD-L1 onto the APD–PD-L1–MIPL, MIP and NIP

APD–PD-L1–MIPL is higher 62% than the MIP, owing to synergism recognition of MIP and the aptamer. In addition, the removal of $CaCO_3$ nanospheres core by acidic eluent enables to reduce stereospecific blockade of binding, and give more binding sites, such as inner cavity and alleviate equilibrium time.

To further conduct the binding ability of the APD–PD-L1–MIPL, MIP and NIP, Freundlich equation was used to depict the binding characteristics, the equation is shown below (6):

$$Q_e = K_F \times C_e^{1/n} \tag{6}$$

where C_e (mg mL^{-1}) is an equilibrium molarity of the binding target, Q_e (mg g^{-1}) is equilibrium adsorption capacity, K_F is binding equilibrium constant, and its binding strength is represented by n^{-1}. In Fig. 2f, g, R^2 of the APD–PD-L1–MIPL and MIP was closer to 1, indicating that this binding process is an inhomogeneous multi-layer binding. According to the regression equation, the binding equilibrium constant KF of the APD–PD-L1–MIPL, MIP and NIP was calculated into 288.2 mg g^{-1},181.1 mg g^{-1} and 72.2 mg g^{-1}, which indicated the existing of plenty of imprinted cavities in the APD–PD-L1–MIPL and MIP, while the adsorption of NIP is mainly non-specific adsorption.

The binding kinetics curves of the APD–PD-L1–MIPL, MIP and NIP are shown in Fig. 2h, and the binding target amount with the MIP is rapidly increased over time, and finally gradually reached balance in 2 h. The Qmax of the APD–PD-L1–MIPL, MIP and NIP were 263.4 mg g^{-1}, 161.3 mg g^{-1} and 63.9 mg g^{-1}. The imprinting factor of the APD–PD-L1–MIPL and MIP in different time was in the range of 2.9–4.9 and 2.4–4.6, respectively (Additional file 1: Fig. S4b).

Various molecularly imprinted polymers including different template molecules and preparation methods in recent years were compared in Table 1. The APD–PD-L1–MIPL excels in terms of adsorption capacity.

Lys, β-CN, BSA, and HRP were selected as competitive protein to assess its selectivity. B-CN (MW 25 kDa, pI 5.8–6.0) has similar molecular weight and isoelectric point to PD-L1 (MW 26.3 kDa, pI 6.4), and the molecular weight and isoelectric point of Lyz (MW 14.5 kDa, pI 9.3), BSA (MW 66 kDa, pI 4.9) and HRP (MW 44 kDa, pI 3–9) are quite different from those factors of PD-L1. In Fig. 3a and Additional file 1: Fig. S4c, the binding characteristic of the APD–PD-L1–MIPL for PD-L1 was about three times as much as any other protein, indicated that the APD–PD-L1–MIPL and MIP has excellent selectivity for PD-L1.

Table 1 Comparison on recently reported molecularly imprinted polymers

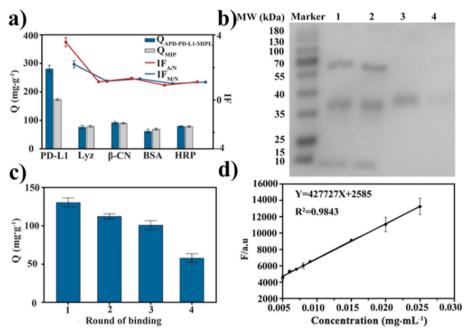| Molecular polymer type	Q_{max}	IF	References
A polydopamine-based molecular imprinted film coating on silica–Fe_3O_4 nanoparticles	4.65 mg g^{-1}	2.19	Jia et al. (2013)
His-tag-anchored epitope imprinting	40 mg g^{-1}	4.26	Li et al. (2015)
Hollow molecularly imprinted polymers using silica nanoparticles as the sacrificial matrix	172.1 mg g^{-1}	2.95	Chen et al. (2019)
Imprinted microspheres with dopamine self-polymerization	266.99 mg g^{-1}	5.45	Zhou et al. (2019)
Core–shell dual-template molecularly imprinted superparamagnetic nanoparticles	73.12 mg g^{-1}	5.54	Gao et al. (2015)
	44.25 mg g^{-1}	4.98	

Fig. 3 **a** Amounts of different proteins bound on the APD–PD-L1–MIPL and MIP. **b** SDS–PAGE analysis of recognition of PD-L1 by MIP NPs: lanes 1 2, protein mixed solution of the APD–PD-L1–MIPL and MIP; lanes 3 4, protein eluate from APD–PD-L1–MIPL and MIP. **c** Reusable of the APD–PD-L1–MIPL. **d** Quantitation of the APD–PD-L1–MIPL. The error bars represent the standard deviation of three independent measurements

To further verify the binding specificity, the APD–PD-L1–MIPL and MIP was added into the mixed protein solution containing Lyz, BSA and PD-L1 protein, respectively, and further analyzed by SDS–PAGE. As shown in Fig. 3b, lanes 1 and 2 represented the protein mixed solution containing Lyz, BSA and PD-L1 before binding ($C_{Lyz} = C_{BSA} = C_{PD-L1} = 0.2$ mg mL^{-1}), and lanes 3 and 4 were eluent of the APD–PD-L1–MIPL and MIP, respectively. PD-L1 band was obviously appeared in the lane of protein eluent, while other stripes can hardly be observed. The bands using the APD–PD-L1–MIPL as recognition templets are darker than MIP, indicating that the APD–PD-L1–MIPL own stronger recognition capacity. In addition, by grayscale analysis of the bands (Additional file 1: Fig. S4d), the PD-L1 protein content was the highest in the eluate bands of the APD–PD-L1–MIPL and MIP. This is further evidence that the eluent mainly was belonged to PD-L1; therefore, both the APD–PD-L1–MIPL and MIP have good selectivity.

The regeneration of the APD–PD-L1–MIPL is also studied, the alternately binding–elution process was repeated four times. As shown in Fig. 3c, the binding PD-L1 quantity fell only slightly about a quarter lower and still maintained high binding capacity after three times (Q were 134,114, and 107 mg g^{-1}, respectively), indicating good regeneration of the APD–PD-L1–MIPL. The binding capacity decreased significantly after the fourth time reuse ($Q = 62$ mg g^{-1}).

Quantitation detection of PD-L1 using the APD–PD-L1–MIP

FITC was applied to conjugate PD-L1 to make the APD–PD-L1–MIPL achieve quantification assay. Protein and FITC were coupled at a mass ratio of 1 mg:150 μg. Then,

they were purified by desalting column to obtain high purity coupling product. $F/P = 2.5$ was calculated, indicating that each mg protein was labeled with 2.5 ug luciferase FITC. In Fig. 3d, a fluorescent intensity increased linearly with the PD-L1 concentration from 0.005 to 0.03 mg mL^{-1}, and the correlation coefficient R^2 was 0.9843, and the limit of detection (LOD) was 0.003 mg mL^{-1}. The limit of detection is obtained by a typical equation 3 σ/s, where σ is the standard error of ten determinations of the blank control trials (dispersion of the APD–PD-L1–MIPL conjugate without PD-L1) and s is the slope corresponding to the linearity of fluorescence.

APD–PD-L1–MIPL inhibit PD-1/PD-L1 engagement of cells

To verify that the APD–PD-L1–MIPL enables specifically bind PD-L1 of the tumor cell, B16 F10 cells with high expression of PD-L1 protein and L-02 cells without PD-L1 protein were selected as model cells and control. The APD–PD-L1–MIPL, MIP and NIP are labeled with FITC. As shown in Fig. 4a, the surface of B16 F10 cells treated with the APD–PD-L1–MIPL showed strong green fluorescence, and the MIP showed relatively weak fluorescence intensity, while NIP NPs can hardly appear fluorescence. On the surface of L-02 cells (Additional file 1: Fig. S5), the APD–PD-L1–MIPL, MIP and NIP present scarcely any green fluorescence. These results indicate that the APD–PD-L1–MIPL and MIP can specifically bind to PD-L1 of cancer cells.

The cytotoxicity of the APD–PD-L1–MIPL, MIP and NIP for L-02 cells and B16 F10 cells was showed that when the concentration of the APD–PD-L1–MIPL, MIP and NIP
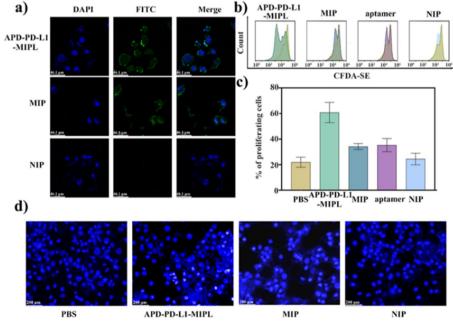

Fig. 4 a Confocal fluorescence imaging of B16 F10 cells after staining with the APD–PD-L1–MIPL, MIP and NIP. The APD–PD-L1–MIPL, MIP, NIP and nuclei are visualized in green and blue, respectively. **b**, **c** Proliferation of T lymphocytes in different groups after staining with CFDA-SE. **d** Imaging of apoptosis of B16 F10 cells after staining with Hoechst 33,258 (blue). The concentration of the APD–PD-L1–MIPL, MIP and NIP was 0.6 mg mL^{-1}, respectively

were lower than 4 mg mL^{-1}, it had no obvious cytotoxicity to L-02 cells and B16 F10 cells (Additional file 1: Fig. S6).

The APD–PD-L1–MIPL is expected to break the binding of PD-1/PD-L1, and promote the proliferation of T lymphocytes. In Fig. 4b, c, the T cell proliferation of PBS group was about 22%, and that of the T cells treated with the APD–PD-L1–MIPL was 61%. In addition, the proliferation of the T cells treated with pure MIP (34.2%) and aptamer (35.3%) group was about 10% higher than that of PBS, while NIP had almost no proliferation effect. This further indicates that the APD–PD-L1–MIPL enable enhance the activity of apoptotic T lymphocytes induced by blocks the binding of PD-1/PD-L1, and significantly stimulate the proliferation of T lymphocytes.

B16 F10 cells were co-cultured with T lymphocytes and using Hoechst 33258 cell staining to observe apoptosis (Fig. 4d). The apoptosis of B16 F10 cells was observed by the nuclear dye Hoechst 33258. The normal nuclei were stained uniform blue, while the apoptotic nuclei showed shrinking state and turned bright blue. In Fig. 4d, after coculturing B16 F10 cells with T lymphocytes, cells in the PBS group showed a uniform blue color, while after the APD–PD-L1–MIPL and MIP treatment, the nuclei turned bright blue. This indicated that the APD–PD-L1–MIPL and MIP could induce apoptosis of B16 F10 cells.

We also performed western blot analysis to know whether the APD–PD-L1–MIPL and MIP could change PD-L1 protein expression in tumor cells. The results (Additional file 1: Fig. S7) showed that the expression level of PD-L1 on the surface of B16 F10 cells did not change significantly after the APD–PD-L1–MIPL and MIP treatment, which indicated that the effects of the APD–PD-L1–MIPL and MIP were similar to "physical resistance", not a drug-induced effect.

For preliminary evaluation feasibility of the APD–PD-L1–MIPL for subsequent intravenous medication, the hemolytic toxicity of the APD–PD-L1–MIPL in the concentration range of 0.2–1 mg mL^{-1} was measured. Results (Additional file 1: Fig. S8) shown that even in the detection range of the highest concentration of hemolytic toxicity is far less than 5%, proving that the APD–PD-L1–MIPL hemolytic toxicity is low, satisfy the requirement of intravenous drugs.

Conclusions

In summary, we successfully fabricated a molecular imprinting polymer modified with aptamer for targeting PD-L1, which can block PD-1/PD-L1 engagement and thus restore tumor killing ability and restrain the further growth of cancer. The prepared APD–PD-L1–MIPL has excellent binding capacity for PD-L1; meanwhile, the presence of aptamer makes its selectivity stronger with dual-targeting functionality. The optimum binding capacity of the APD–PD-L1–MIPL is 266.8 mg g^{-1}, and the best IF is exceeded to 4.2. The APD–PD-L1–MIPL has good specificity for PD-L1, as confirmed by confocal fluorescent imaging and inhibited of tumor immune escape. The APD–PD-L1–MIPL can also be used to determine the amounts of the components of PD-L1 with LOD of 0.003 mg mL^{-1}. The proliferation of T lymphocytes and cell apoptosis further demonstrated that the APD–PD-L1–MIPL and MIP could inhibit the activity of cancer cells. Although the APD–PD-L1–MIPL could be difficulty in the practical uses for drug penetration, because the tumor microenvironment is denser than the extracellular matrix

of normal tissues, we have faith in that this way can boost the development of immuno-therapy and will adapt to other targets.

Supplementary Information

The online version contains supplementary material available at https://doi.org/10.1186/s12645-023-00209-3.

> **Additional file 1.** Supplementary information.

Declarations

Competing interests
The authors declare no competing interests.

References
Bellmunt J, Powles T, Vogelzang NJ (2017) A review on the evolution of PD-1/PD-L1 immunotherapy for bladder cancer: the future is now. Cancer Treat Rev 54:58–67

Borghaei H, Paz-Ares L, Horn L, Spigel DR, Steins M, Ready NE et al (2015) Nivolumab versus docetaxel in advanced nonsquamous non-small-cell lung cancer. N Engl J Med 373(17):1627–1639

Callahan MK, Wolchok JD (2013) At the bedside: CTLA-4- and PD-1-blocking antibodies in cancer immunotherapy. J Leukoc Biol 94(1):41–53

Chen L, Li DQ, Zhong J, Wu XL, Chen Q, Peng H et al (2011) IL-17RA aptamer-mediated repression of IL-6 inhibits synovium inflammation in a murine model of osteoarthritis. Osteoarthrit Cartil 19(6):711–718

Chen W, Fu M, Zhu X, Liu Q (2019) Protein recognition by polydopamine-based molecularly imprinted hollow spheres. Biosens Bioelectron 142:111492

de Filette J, Andreescu CE, Cools F, Bravenboer B, Velkeniers B (2019) A systematic review and meta-analysis of endocrine-related adverse events associated with immune checkpoint inhibitors. Horm Metab Res 51(3):145–156

Dong Z, Feng L, Hao Y, Chen M, Gao M, Chao Y et al (2018) Synthesis of hollow biomineralized $CaCO_{(3)}$-polydopamine nanoparticles for multimodal imaging-guided cancer photodynamic therapy with reduced skin photosensitivity. J Am Chem Soc 140(6):2165–2178

Gao RX, Zhao SQ, Hao Y, Zhang LL (2015) Synthesis of magnetic dual-template molecularly imprinted nanoparticles for the specific removal of two high-abundance proteins simultaneously in blood plasma. J Sep Sci 38(22):3914–3920

Gu Z, Dong Y, Xu S, Wang L, Liu Z (2021) Molecularly imprinted polymer-based smart prodrug delivery system for specific targeting, prolonged retention, and tumor microenvironment-triggered release. Angew Chem Int Ed Engl 60(5):2663–2667

Guo Z, Xing R, Zhao M, Li Y, Lu H, Liu Z (2021) Controllable engineering and functionalizing of nanoparticles for targeting specific proteins towards biomedical applications. Adv Sci (weinh) 8(24):e2101713

Hao Y, Gao R, Liu D, He G, Tang Y, Guo Z (2016) A facile and general approach for preparation of glycoprotein-imprinted magnetic nanoparticles with synergistic selectivity. Talanta 153:211–220

Haupt K, Medina Rangel PX, Bui BTS (2020) Molecularly imprinted polymers: antibody mimics for bioimaging and therapy. Chem Rev 120(17):9554–9582

Jia X, Xu M, Wang Y, Ran D, Yang S, Zhang M (2013) Polydopamine-based molecular imprinting on silica-modified magnetic nanoparticles for recognition and separation of bovine hemoglobin. Analyst 138(2):651–658

Kato K, Ikeda H, Miyakawa S, Futakawa S, Nonaka Y, Fujiwara M et al (2016) Structural basis for specific inhibition of Autotaxin by a DNA aptamer. Nat Struct Mol Biol 23(5):395–401

Kimani M, Beyer S, El-Schich Z, Gawlitza K, Gjorloff-Wingren A, Rurack K (2021) Imprinted particles for direct fluorescence detection of sialic acid in polar media and on cancer cells with enhanced control of nonspecific binding. ACS Appl Polym Mater 3(5):2363–2373

Lai WY, Huang BT, Wang JW, Lin PY, Yang PC (2016) A novel PD-L1-targeting antagonistic DNA aptamer with antitumor effects. Mol Ther Nucl Acids 5(12):e397

Lao YH, Phua KK, Leong KW (2015) Aptamer nanomedicine for cancer therapeutics: barriers and potential for translation. ACS Nano 9(3):2235–2254

Li SW, Yang KG, Liu JX, Jiang B, Zhang LH (2015) Surface-imprinted nanoparticles prepared with a His-tag-anchored epitope as the template. Anal Chem 87(9):4617–4620

Li X, Shao C, Shi Y, Han W (2018) Lessons learned from the blockade of immune checkpoints in cancer immunotherapy. J Hematol Oncol 11(1):31

Liu R, Poma A (2021) Advances in molecularly imprinted polymers as drug delivery systems. Molecules 26(12):1

Mahoney KM, Rennert PD, Freeman GJ (2015) Combination cancer immunotherapy and new immunomodulatory targets. Nat Rev Drug Discov 14(8):561–584

Mayer G (2009) The chemical biology of aptamers. Angew Chem Int Ed Engl 48(15):2672–2689

Minouraa N, Rachkov A, Higuchi M, Shimizu T (2001) Study of the factors influencing peak asymmetry on chromatography using a molecularly imprinted polymer prepared by the epitope approach. Bioseparation 10(6):399–407

Ng EW, Shima DT, Calias P, Cunningham ET Jr, Guyer DR, Adamis AP (2006) Pegaptanib, a targeted anti-VEGF aptamer for ocular vascular disease. Nat Rev Drug Discov 5(2):123–132

Pan J, Yao H, Guan W, Ou H, Huo P, Wang X et al (2011) Selective adsorption of 2,6-dichlorophenol by surface imprinted polymers using polyaniline/silica gel composites as functional support: equilibrium, kinetics, thermodynamics modeling. Chem Eng J 172(2–3):847–855

Qian L, Liu W, Liu H, Nica V, Zhang S, Zhou Q et al (2021) Fabrication of raspberry-like cytochrome C surface-imprinted nanoparticles based on MOF composites for high-performance protein separation. ACS Appl Mater Interfaces 13(26):31010–31020

Robert C, Schachter J, Long GV, Arance A, Grob JJ, Mortier L et al (2015) Pembrolizumab versus ipilimumab in advanced melanoma. N Engl J Med 372(26):2521–2532

Saleh R, Elkord E (2020) Acquired resistance to cancer immunotherapy: role of tumor-mediated immunosuppression. Semin Cancer Biol 65:13–27

Sun H, Zhu X, Lu PY, Rosato RR, Tan W, Zu Y (2014) Oligonucleotide aptamers: new tools for targeted cancer therapy. Mol Ther Nucl Acids 3(8):e182

Wackerlig J, Schirhagl R (2016) Applications of molecularly imprinted polymer nanoparticles and their advances toward industrial use: a review. Anal Chem 88(1):250–261

Wheeler LA, Trifonova R, Vrbanac V, Basar E, McKernan S, Zhan X et al (2011) Inhibition of HIV transmission in human cervicovaginal explants and humanized mice using CD4 aptamer-siRNA chimeras. J Clin Invest 121(6):2401–2412

Zak KM, Kitel R, Przetocka S, Golik P, Guzik K, Musielak B et al (2015) Structure of the complex of human programmed death 1, PD-1, and its ligand PD-L1. Structure 23(12):2341–2348

Zhao H, Zhang Z, Zuo D, Li L, Li F, Yang D (2021a) A synergistic DNA-polydopamine-MnO$_2$ nanocomplex for near-infrared-light-powered DNAzyme-mediated gene therapy. Nano Lett 21(12):5377–5385

Zhao W, Xiaochun H, Li W, Li R, Chen J, Zhou L et al (2021b) M2-like TAMs function reversal contributes to breast cancer eradication by combination dual immune checkpoint blockade and photothermal therapy. Small 17(13):2007051

Zhou JJ, Wang YF, Bu J, Zhang BL, Zhang QY (2019) Ni-BSA directional coordination-assisted magnetic molecularly imprinted microspheres with enhanced specific rebinding to target proteins. ACS Appl Mater Interfaces 11(29):25682–25690

Zhu R, Zhao W, Zhai M, Wei F, Cai Z, Sheng N et al (2010) Molecularly imprinted layer-coated silica nanoparticles for selective solid-phase extraction of bisphenol A from chemical cleansing and cosmetics samples. Anal Chim Acta 658(2):209–216

Zou W, Wolchok JD, Chen L (2016) PD-L1 (B7–H1) and PD-1 pathway blockade for cancer therapy: mechanisms, response biomarkers, and combinations. Sci Transl Med 8(328):328rv324

Publisher's Note